J Mater Sci (2006) 41:8320–8328
DOI 10.1007/s10853-006-1017-4

Structural and morphological properties of RE^{3+} doped sesquioxide Y_2O_3 spherical nanoparticles

W. A. Kaczmarek · H. Riesen

Received: 9 June 2004 / Accepted: 23 September 2005 / Published online: 11 November 2006

Abstract Effects of rare earth (Er^{3+}, Yb^{3+}, Sm^{3+}, Ce^{3+}) doping of yttrium oxide nanoparticles on the crystal structure and morphology have been investigated. X-ray diffraction, thermal analysis and scanning electron microscopy show that chemical and structural transformations are taking place in as-prepared carbonate spherical particles in the temperature range of 400–1200 K. In the final form crystalline agglomerates are compositionally homogeneous with a diameter range of 165–185 nm and an average crystalline grain size of 45 nm. Rare earth (RE) doped yttria particles are found to be up to 40% smaller in crystal grain size. The development of surface texture is due to nanocrystalline substructure which is related to the applied thermal treatment: carbonate decomposition and yttria crystallization processes.

Introduction

The world of engineering and technology has entered a new period where the continuation of electronic device miniaturization is mainly limited by the availability of suitable functional materials. Due to their rich physical properties, crystalline oxides in form of thin films or particulate media can be used in many applications, offering solutions to a number of challenging problems in the rapidly evolving field of microelectronics. However, the quality and functionality of metal oxide materials depend critically on the type of manufacturing process applied. It is well understood that the presence of macro and micro-defects in the final product will cause intolerable parameter variations, producing reliability degradation for future applications. In particular, applications of nano-circuits and nano-sensors based on metal oxide dielectric materials suffer from the increased presence of charge defects located on the surface or near the interface. These defects can produce excessive photon and/or electron scattering, leading to a deterioration of photonic and electronic parameters of such devices.

The sesquioxide α-Y_2O_3 (yttria) is an example of a material, which has attracted much attention because of several relevant physical properties such as its extreme crystallographic phase stability up to about 2600 K, where it transforms into the high temperature β-Y_2O_3 form [1], high thermal conductivity and high refractive index $n = 1.9$ [2]. With many industrial products based on high thermodynamical durability of bulk ceramics made from yttria, the area of possible applications in microelectronics as reliable photonic material was extended significantly during the last decade. In particular, yttrium oxide based films and particles are extensively studied as replacement of conventional red-green-blue (RGB) phosphors used for cathode ray tubes (CRT); the reason for this is that the conventional materials are not applicable to a new type of field-emission display (FED) technology [3–4]. Typical examples of such alternative materials are based on yttria doped separately with Sm^{3+}, Er^{3+}, Ce^{3+}, Eu^{3+}, Tb^{3+} and Tm^{3+} ions. For these materials maximum

W. A. Kaczmarek (✉) · H. Riesen
School of Physical, Environmental and Mathematical Sciences, University College, The University of New South Wales, Australian Defence Force Academy, Canberra, ACT 2600, Australia
e-mail: w.kaczmarek@adfa.edu.au

luminescence efficiencies can be observed with rare-earth concentrations in the range between 0.5 and 10 at% [5–6]. For such applications the development of new materials and detailed studies of structure and morphology are important.

Yttria based RE^{3+} doped materials have been synthesized in different forms: monocrystals [7], polycrystalline powders [8], micro- or nano-crystalline films [9]. In the case of powders, a variety of preparation methods such as the traditional dry ceramic method based on solid-state decomposition reactions [10] and several kinds of wet-chemical approaches have been used in preparation, including low temperature urea based homogeneous precipitation [11–12], oxalate co-precipitation [13], ammonium carbonate assisted precipitation [14], high temperature glycol-nitrate combustion [15], spray pyrolysis [16], microemulsion-microwave heating [17] or the solvothermal method [18]. The wet-chemically derived yttria based oxides generally show a final product of better quality with finer particle and crystalline size than those obtained via solid-state reactions. However to our knowledge, little attention has been paid to the investigation of the modifications of the structural and morphological properties of the particles as a result of the crystallization process when annealing was applied.

Recently, we undertook a systematic study of the conditions of growth of rare earth doped yttrium oxide particles. In all our preparations we adopted a low temperature precipitation method followed by high temperature annealing. The present paper reports our work on preparation aspects as well as structural and morphological characteristics of the synthesized particles.

Experimental

RE^{3+} doped yttrium oxide powders were obtained by adopting the procedure outlined by Matijevic and Hsu for lanthanide compounds [11], and later extended also to mixed systems by Aiken et al. [12]. The original work on the precipitation of lanthanides from water solutions of nitrates and chlorides with urea has shown the way to produce a variety of particle shapes. In particular our attention has been directed to the well-known decomposition of urea in aqueous media at temperatures up to 100°C which yields ammonium and cyanate ions [19].

$$H_2N - CO - NH_2 \rightarrow NH_4^+ + OCN^- \quad (1)$$

In acidic solution, the cyanate ions decompose rapidly into carbon dioxide and ammonium ions according to

$$OCN^- + 2H^+ + H_2O \rightarrow CO_2 + NH_4^+ \quad (2)$$

but in neutral or basic solutions ammonia and carbonate ions are formed.

$$OCN^- + OH^- + H_2O \rightarrow NH_3 + CO_3^{2-} \quad (3)$$

The urea decomposition reaction (Eq. (1)) is extremely slow, but can be accelerated in the presence of metal ions. Most M^{3+} metal ions lead to slight hydrolysis [20]:

$$M(H_2O)_n^{3+} + H_2O \leftrightarrow [M(OH)(H_2O)_{n-1}]^{2+} + H_3O^+ \quad (4)$$

For the above reaction the equilibrium shifts to the right with increasing atomic number of the metal M (for yttrium and all lanthanides) [11]. In case of aqueous solutions of yttrium nitrate and urea the precipitation of the basic carbonate proceeds then according to the following overall mass balanced equation in the temperature range of 360–373 K:

$$YOH(H_2O)_{n-1}]^{2+} + CO_3^{2-} \rightarrow Y(OH)CO_3 \cdot H_2O + (n-2)H_2O \quad (5)$$

The release of carbonate ions by the urea decomposition is controlled by temperature; once the critical value of ~ 360 K is reached precipitation starts. From Eq. (2) and (3) it follows that the precipitation process for urea-metal nitrate solutions is best done under acidic conditions.

In acidic solutions it can also be expected that an additional reaction step will take place during the urea decomposition, namely the weak formation of carbonic acid according to Eq. (6).

$$OCN^- + 2H^+ + 2H_2O \rightarrow NH_4^+ + H_2CO_3 \quad (6)$$

The isoelectric point of the basic carbonate particle surface is at pH = 7.6. Thus it is favorable to conduct the urea decomposition in the lower pH range [11], since precipitating particles are charged slightly positively below this value. Hence electrostatic repulsion will discourage agglomeration of the precipitated solids. Thus in all our preparations we adjusted the pH of the initial aqueous solutions within a range of 5.5–6. However, the control of the pH value during the decomposition phase is difficult because of the elevated temperature. As we mentioned above, the urea decomposition is extremely slow even at temperatures close to 373 K (estimated ratio of 4% per hour [19]). Thus the amount of urea molecules needed to reach a critical CO_3^{2-} ion saturation within a given period of

time must be much higher than the overall stochiometric amount of Y^{3+} and RE^{3+} ions. Hence, in all preparations described in this report the starting molar ratio of urea to (Y^{3+} and RE^{3+}) ion has been set to the value of 20:1. The optimum conditions for spherical particle formation were set to initial concentrations of 0.6 mol/dm^3 urea and 0.03 mol/dm^3 yttrium nitrate $Y(NO_3)_3$ according to an earlier study [11]. The addition of RE^{3+} ions has been calculated according to the required yttrium substitution. Most of our powders were precipitated under similar conditions: 1 dm^3 starting solution and total aging time of 2 h at a temperature of 365 K. The synthesized materials were rinsed with the same volume of distilled water, centrifuged (five times) and finally dried at 370 K. All preparations were based on analytical grade reagents from Aldrich: yttrium nitrate $Y(NO_3)_3{\cdot}6H_2O$, 99.9%), erbium chloride ($ErCl_3{\cdot}6H_2O$, 99.9+%), ytterbium chloride ($YbCl_3{\cdot}6H_2O$, purity 99.998%), samarium chloride ($SmCl_3{\cdot}6H_2O$, 99+%), chromium nitrate ($Cr(NO_3)_3{\cdot}9H_2O$ 99.99+%) and urea (CH_4N_2O, 99+%).

The chemical compositions for all as-prepared and annealed powders are listed in Table 1. The precipitates (as-prepared powders) were calcined at 1100 K for 1 h in an electric muffle furnace. In addition, some of the crystalline powders were also annealed in a tubular furnace in flowing hydrogen (0.1 dm^3/min) to study redox properties and associated changes in optical properties.

The final products were characterized by X-ray diffraction (XRD) with Cu K_α radiation (λ = 0.15418 nm), using a Sietronics SIE 122D diffractometer equipped with a Philips goniometer. All XRD spectra

Table 1 Composition and structural properties of as-prepared and annealed powders

Sample Code	Chemical Composition	Annealing	Structure Type	L (nm)
Y-AP	$Y(OH)CO_3$	–	AM	–
Y-AN700	$Y(OH)CO_3$	1 h at 700 K	AM	
Y-AN889	$Y(OH)CO_3$ and Y_2O_3	10 min at 889 K	CR - Multiphase	16
Y-AN929	$Y(OH)CO_3$ and Y_2O_3	10 min at 929 K	CR - Multiphase	24
Y-AN	Y_2O_3	1 h at 1100 K	CR -cubic	45
Y-AN-H	Y_2O_3	1 h at 1100 K (Air+H)	CR -cubic	43
Cr-AP	$Y(OH)CO_3$:1%Cr	–	AM	–
Cr-AN	Y_2O_3:1%Cr	1 h at 1100 K	CR -cubic	24
Er1-AP	$Y(OH)CO_3$:1%Er	–	AM	–
Er1-AN	Y_2O_3:1%Er	1 h at 1100 K	CR - cubic	45
ErYb2-AP	$Y(OH)CO_3$:1%Er+2%Yb	–	AM	–
ErYb2-AN	Y_2O_3:1%Er+2%Yb	1 h at 1100 K	CR -cubic	43
ErYb4-AP	$Y(OH)CO_3$:1%Er+4%Yb	–	AM	–
ErYb4-AN	Y_2O_3:1%Er+4%Yb	1 h at 1100 K	CR -cubic	34
ErYb6-AP	$Y(OH)CO_3$:1%Er+6%Yb	–	AM	–
ErYb6-AN	Y_2O_3:1%Er+6%Yb	1 h at 1100 K	CR -cubic	33
ErYb8-AP	$Y(OH)CO_3$:1%Er+8%Yb	–	AM	–
ErYb8-AN	Y_2O_3:1%Er+8%Yb	1 h at 1100 K	CR -cubic	34
ErYb10-AP	$Y(OH)CO_3$:1%Er+10%Yb	–	AM	–
ErYb10-AN	Y_2O_3:1%Er+10%Yb	1 h at 1100 K	CR -cubic	37
Yb1-AP	$Y(OH)CO_3$:1%Yb	–	AM	–
Yb1-AN	Y_2O_3:1%Yb	1 h at 1100 K	CR -cubic	32
Yb4-AP	$Y(OH)CO_3$:4%Yb	–	AM	–
Yb4-AN	Y_2O_3:4%Yb	1 h at 1100 K	CR -cubic	33
Sm1-AP	$Y(OH)CO_3$:1% Sm	–	AM	–
Sm1-AN	Y_2O_3:1% Sm	1 h at 1100 K	CR -cubic	35
Sm-AN-H	Y_2O_3:1% Sm	1 h at 1100 K (Air +H)	CR -cubic	33
Sm3-AP	$Y(OH)CO_3$:3% Sm	–	AM	–
Sm3-AN	Y_2O_3:3% Sm	1 h at 1100 K	CR -cubic	32
SmCe2-AP	$Y(OH)CO_3$:1%Sm+2%Ce	–	AM	–
SmCe2-AN	Y_2O_3:1%Sm+2%Ce	1 h at 1100 K	CR -cubic	28
Sm5Ti5-AP	$Sm_2(CO_3)_3{\cdot}3H_2O$),$Y_2(CO_3)_3{\cdot}2H_2O$ and TiO_2	–	AM and CR	50
Sm5Ti5-AN800	Y_2O_3:5%Sm+5%Ti	1 h at 800 K	AM	
Sm5Ti5-AN	Y_2O_3:5%Sm + $Y_2Ti_2O_7$	1 h at 1100 K	CR - Multiphase	57
Sm5Ti5-AN-H	Y_2O_3:5%Sm + $Y_2Ti_2O_7$	1 h at 1100 K (Air +H)	CR - Multiphase	57

The structure type column describes the crystallographic phase of the materials: CR – crystalline, AM – amorphous. The letter H denotes samples that were annealed in flowing hydrogen gas. The L value is the diameter of the average crystal grain estimated from the strongest XRD peak for annealed powders. Most L values have been calculated using the most intense peak of the α –Y_2O_3 cubic phase

were acquired with a 2θ range of 15–75° and a scan rate of 1 deg/min. The structure determination was supported by the application of JCPDS-ICDD database software. The particle morphology was examined by direct observation of platinum-coated samples on a Hitachi S-4500 field emission scanning electron microscope (FESEM) with a maximum possible magnification of × 500 K. The calorimetric and thermogravimetric experiments were performed employing a NETZSCH STA 449 Jupiter thermal analyzer, which is capable to perform simultaneous measurements of mass change and transformation energies. The STA 449 software allowed the computation of temperature dependent parameters such as: the mass change (TG), rate of mass change (DTG), mass change steps, onset and peak temperatures, and heat flow rate (DSC). TG-DSC type S sensors as well as platinum crucibles were used for the thermal measurements. The samples were air heated from room temperature up to ~1315 K at a heating rate of 10 K/min.

Results and discussion

The chemical composition and some structural information of all as-prepared and calcined powders are presented in Table 1.

XRD analysis

Representative X-ray diffraction patterns of as-prepared and annealed powders are presented in Figs. 1, 2 and 3. The as-prepared $Y(OH)CO_3$ powder is amorphous as follows from the XRD pattern shown in Fig. 1. This has been found to be typical for all precipitated and samples dried at temperatures below 370 K. The diffraction pattern shows two very broad features centered at $2\theta = 31° \pm 1°$ and $2\theta = 47° \pm 1°$ with full widths at half maximum (FWHM) of $7° \pm 0.5°$ and $11° \pm 0.5°$, respectively. The same features but with slightly increased peak intensities are also visible for samples annealed in air at temperatures up to 700 K and for as long as 1 h. We note that this kind of behavior is an indication of a relatively stable amorphous phase up to this temperature. This is an interesting result and further discussion is included in Thermal Analysis section. A completely crystalline material is obtained after calcination at 1100 K in air for 1 h and the XRD pattern shows the characteristic reflections associated with a cubic type structure. A detailed analysis of the XRD patterns allowed for an indexing of all discernible peaks. Moreover, it follows

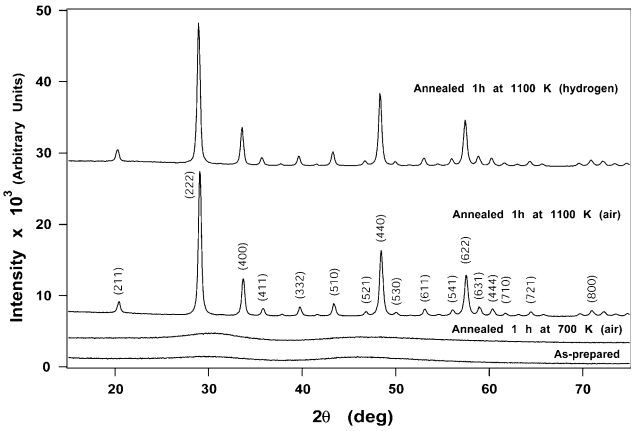

Fig. 1 XRD patterns of as-prepared $Y(OH)CO_3$ powder and samples following a 1 h annealing period at indicated temperatures and atmospheres

also that only one crystalline α-Y_2O_3 phase, having a cubic bixbyite structure with space group $Ia3$ (T_h^7) [21], is present. For all XRD patterns of crystalline materials excellent agreement has been found with the JCPDS database reference card number 05-0574.

The appearance of the cubic crystalline yttria phase as the main component in powders after annealing at high temperature can be expected and is well understood in terms of dehydration and decarbonation processes taking place in the initial $Y(OH)CO_3$ material.

Supplementary annealing in flowing pure hydrogen gas has a minimal effect on the XRD patterns recorded for crystalline powders: the cubic structure characteristic for yttria prevails and only the FWHM of the diffraction peaks increase slightly. As a result, the estimated value of the average crystal grain size decreases slightly from 45 nm to 43 nm, but we note here that this reduction is in the error range of ± 10%. Visual examination of the resulting powders showed a change in powder color from white to gray; the same occurred for all other powders subject to the same treatment. The color change indicates that a partial reduction takes place in the yttria nanocrystals, pointing to a stable crystal structure with the formation of permanent oxygen vacancies. Recently, to further investigate this effect in more detail, an additional microstructural analysis based on high-resolution electron energy loss spectroscopy (HR EELS) has been performed on the same samples. The EELS results confirm the above assumption and will be reported separately.

Figure 2 shows the XRD pattern obtained for powders annealed for a relatively short time of 10 min at temperatures of 889 K and 929 K, respectively. These two temperatures were estimated as starting

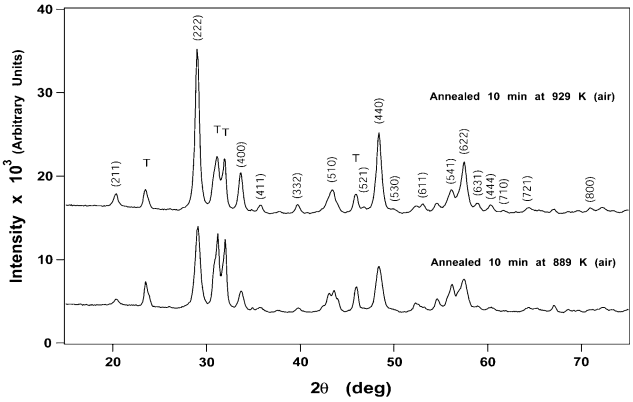

Fig. 2 XRD patterns of annealed $Y(OH)CO_3$ powders showing crystallization of the Y_2O_3 cubic phase (indexed). Additional XRD peaks are attributed to a low temperature crystalline transition phase (marked here by *T*)

and finishing points of the exothermic DSC peak (see Fig. 4). As a result of different annealing procedure (static or dynamic) for the samples investigated by XRD and DSC methods, only a qualitative analysis of the diffraction patterns in Fig. 2 can be given. For both samples the recorded patterns show peaks characteristic for multiphase crystalline materials. A difference in XRD peak intensities is well visible for the two samples. It is clear that in the powder annealed at 889 K crystallization of the main cubic α-Y_2O_3 phase initiates and is close to completion for the sample annealed at 929 K. With increasing annealing temperature the relative XRD peak intensities of the cubic phase increase. At this stage the composition and structure of the phase existing between the amorphous and cubic structures is uncertain, but our results point to some form of crystalline yttrium carbonate. In Fig. 2 the letter T has been used to mark peaks related to this transitional crystalline phase and the remaining peaks have been attributed to the crystalline yttria phase. The present XRD results for $Y(OH)CO_3$ powders are in excellent agreement with data from thermal analysis as is discussed in Section 3.2.

The average crystal grain size has been estimated from the strongest peak (222) of the cubic phase by applying the Scherrer equation: $L = K\lambda/\beta\cos\theta$ where K is the shape factor ($K = 0.94$), λ is the X-ray wavelength ($\lambda = 0.154$ nm), θ is the Bragg angle and β is the pure instrumental line broadening. Table 1 shows estimated values of the crystal grain size for all samples. The size shows clearly a variation, even when taking into account that the error in the L value estimation can be as high as ±10% [22]. By comparing the L values for all doped yttria powders to the value of undoped crystalline Y_2O_3 powders ($L = 45$ nm) it follows that larger crystal grains were only obtained for the material doped with 5% of Sm^{3+} and 5% of Ti^{3+}. All other powders showed noticeable lower L values. We expect that such large L value have to be directly related to highest concentration of Sm^{3+} and Ti^{3+} ions in the yttria host structure. A higher concentration of titanium in particular can have a rather significant effect on the cubic phase XRD peaks broadening: the formation of a second crystalline phase has been found in this material. Yttria doped with 1% Cr^{3+} shows no additional crystalline phase formation. This may be due to the lower concentration of the impurity.

Figure 3 shows the evolution of the XRD pattern for $Y(OH)CO_3$:5%Sm5%Ti as a function of annealing conditions. Surprisingly, the diffraction pattern recorded for the as-prepared powder shows XRD peaks characteristic for a polycrystalline material. As we mentioned in experimental part not all as-prepared powders were dried at 370 K. The powder in Fig. 3 has been fast dried after synthesis at $T \approx 450$ K in which rapid water loss occurs. As a result, crystallization of hydrated forms of samarium carbonate ($Sm_2(CO_3)_3 \cdot 3H_2O$) and yttrium carbonate ($Y_2(CO_3)_3 \cdot 2H_2O$) phases have been observed. The estimated average crystal grain size has been found to be 50 nm. Parallel with these two crystalline components, additional broad features in the XRD pattern are also noticeable. This points to the presence of a third phase, possibly amorphous titanium oxide (TiO_2). The overall intensity of the broad XRD peaks in this phase has been found to be very low which is in accord with an expected contribution from 5% of Ti.

Annealing at 800 K for 1 h yields a material with an XRD pattern that is characteristic of an amorphous

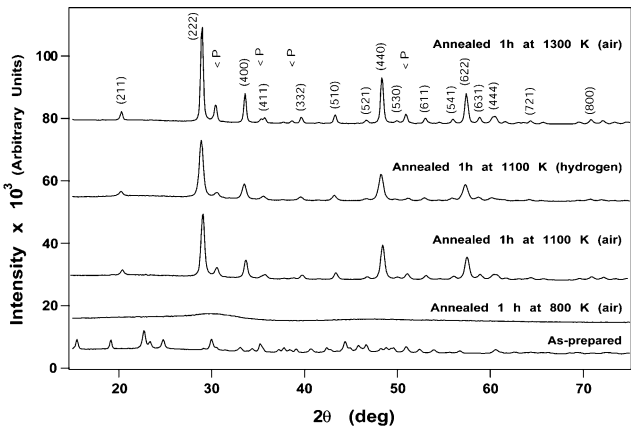

Fig. 3 XRD patterns of as-prepared $Y(OH)CO_3$:5%Sm5%Ti powder and following 1 h annealing at indicated temperatures and atmosphere

material. This rather unexpected result can be explained only on the basis of thermal stability characteristics of crystalline samarium and yttrium carbonates. In the lower temperature range both carbonates form stable crystalline structures but at higher temperatures chemical and structural decomposition are taking place. A similar effect has been reported for rod-like yttrium carbonate particles [12]. With the temperature approaching 800 K former crystalline phases recede and are replaced by an amorphous state. We assume that this disordered material incorporates amorphous forms of oxides (Y_2O_3,Sm_2O_3 and TiO_2). By comparison with the undoped Y_2O_3 sample (see above) T = 800 K is ~90° below the yttria crystallization temperature and as a result the yttria phase is not visible in the diffraction pattern. Further annealing steps, performed in air at 1100 K and 1300 K, produce a fully crystalline material with characteristic diffraction patterns presented in the top part of Fig. 3. There is only a marginal difference in XRD peak intensities between the two spectra and the calculated value of crystal grain size is L = 57 nm in each case. The idea behind the synthesis of the $Y(OH)CO_3$:5%Sm5%Ti powder was to obtain an efficient spectral hole-burning material that is based on Sm^{2+} ions in the yttria structure. The Ti^{4+} ions should then stabilize the Sm^{2+} via charge compensation. However, the XRD results presented here for the annealed samples suggest the presence of a material with compositional phase segregation built on two major crystalline phases: Y_2O_3:5%Sm and $Y_2Ti_2O_7$. The first phase has the cubic yttria structure where part of Y^{3+} ions are replaced by Sm^{3+} ions. The second crystalline phase is a pyrochlore type that is a derivative of the fluorite structure. In fact, according to the previous study for this particular pyrochlore, the chemical formula can be expressed in terms of a mixture of two oxides $Y_2O_3(TiO_2)_2$ and this material has a high thermodynamic stability [23]. In our sample, as a result of the yttria and pyrochlore phase separation, any charge compensation of the type $Sm^{2+} \leftrightarrow Ti^{4+}$ taking place between crystal grains is unlikely. Thus our attempt to synthesize an efficient hole-burning material based on active Sm^{2+} ions failed.

The preparation of the $Y(OH)CO_3$:5%Sm5%Ti powder described here shows a pronounced tendency of crystalline yttria to incorporate RE^{3+} ions. In contrast titanium ions appear to be not suitable to replace yttrium ions in the cubic structure, resulting in the formation of a second crystalline phase (our other preparations using Zr or Al compounds showed the same effect as for Ti). This particular trend is based on the ionic radii of trivalent rare earth ions, which are close to or slightly larger than the radius of Y^{3+} (0.0893 nm). In case of Ti^{3+} ions the situation for possible Ti → Y replacement is radically different; the crystal ionic radii of Ti ions are 24% or 15% smaller (0.068 for Ti^{4+} and 0.076 nm for Ti^{3+}). Moreover, we stress here that the cubic system is characteristic for all rare earth oxides. In contrast, titanium oxides form crystals in tetragonal and hexagonal structures.

Thermal analysis

The first differential thermal analysis (DTA) data for yttrium carbonate have been published by Aiken et al. [12]. The reported data is not conclusive but some recent reports still follow up on these partial findings [24]. New results obtained from thermal analysis measurements for $Y(OH)CO_3$ powder are presented in Fig. 4. The thermogravimetric (TG) scan shows characteristic features for a sample containing (=CO) and (–OH) groups.

The first mass change step (–9.72%) occurs at low temperature, ending at ~560 K, and is associated with a significant change in chemical composition. In parallel, the DSC endothermic peak in this temperature range is characteristic of a thermal decomposition process in which (–OH) groups are removed from the starting material. A dehydration process requires an increased quantity of energy and the measured heat flow in this range of 235.7 J/g is the largest in the measured temperature range for the $Y(OH)CO_3$ powder. The remaining material, still in an amorphous form, undergoes additional transformations with two mass loss steps of –8.50% and –6.20% respectively. During the

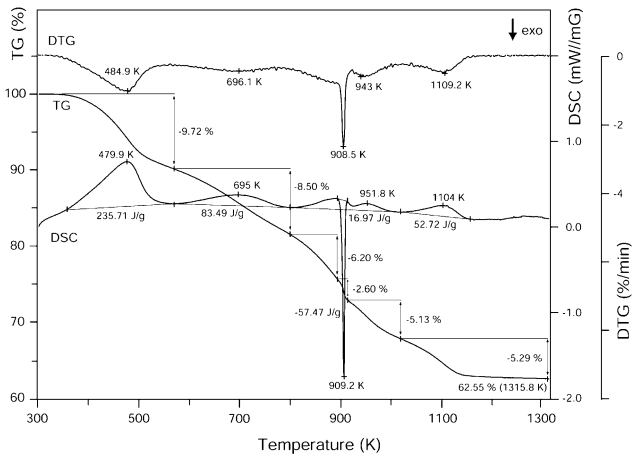

Fig. 4 Temperature-dependent mass change (TG), rate of mass change (DTG) and heat flow rate (DSC) recorded for a $Y(OH)CO_3$ sample

latter step above ~700 K, formation of the transitional crystalline phase is taking place and the recorded DSC curve for this region shows only one rather small endothermic peak centered at 695 K. The fourth mass loss is the smallest and occurs in the temperature range between 889 K and 929 K. A sharp exothermic DSC peak accompanies this step. From XRD measurement it was concluded that in the vicinity of ~886 K crystallization of the cubic yttria phase initiates and at ~929 K is close to completion. The energy flow for this temperature range is –57.4 J/g and the observed minimum value of the DSC peak is at 909.2 K, which corresponds well to the temperature where the maximum rate of mass change occurs. The final two mass changes (in total –10.4%) are taking place between ~930 K and ~1130 K. Decomposition of a material in such a high temperature range is rather surprising and an explanation cannot be directly deduced only from the thermal analysis data. At the present moment it is difficult to discuss this ''high temperature'' form of a carbonate. As before we can assume that formation of cubic yttria fine nanocrystals at temperatures around 900 K is not the final crystallization step, rather it must be accompanied by further decomposition of yttrium carbonate with increasing yttria crystal grain size. From TG and DSC curve shapes reported in Fig. 4 it can be concluded that the crystalline and thermodynamically stable yttria phase occurs at temperatures above ~1100 K which is in contrast with earlier claims about full crystallization at temperatures above 913 K [12].

SEM analysis

Scanning electron microscopy (SEM) analysis of as-prepared and annealed samples has been performed for the majority of samples that are summarized in Table 1. In general all SEM results show similar morphological characteristics and thus only selected micrographs are shown in the present report. Figure5 shows micrographs of four powders with the starting composition of yttrium carbonate ($Y(OH)CO_3$) described as AP. Other powders were coded in a similar way (see Table 1 entry for Y-AP), AN7 (Y-APN), AN (Y-AN) and AN+H (Y-AN-H). Applied magnifications of 30 k and 100 k have been chosen to show morphological details. All particles appear to be very similar with a characteristic spherical shape. We note that the powder samples consist of agglomerated particles that share a very narrow range of the particle size distribution. This kind of particle shape has been expected as a consequence of the preparation conditions that were followed. For the as-prepared sample (AP) the diameter of synthesized

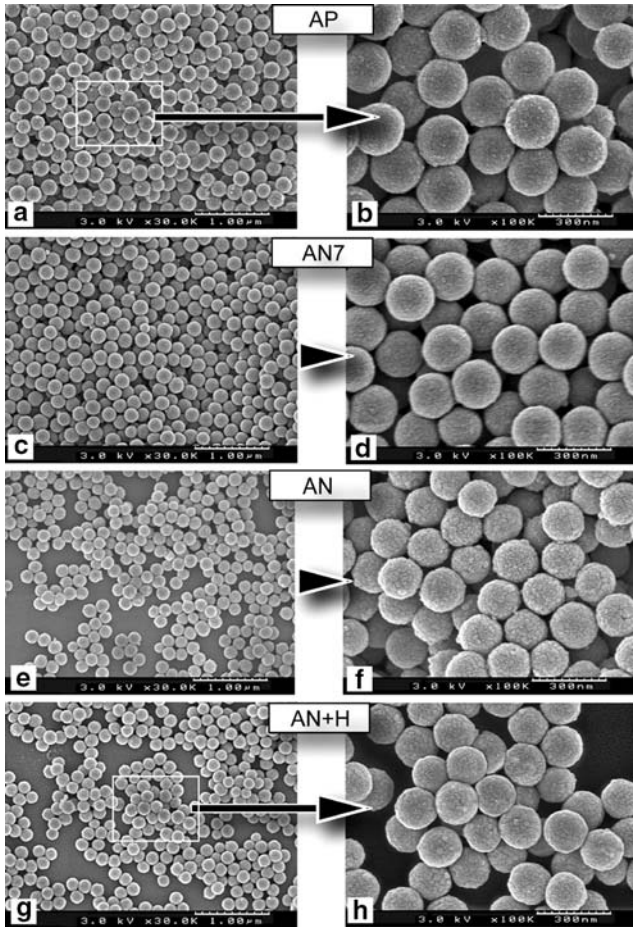

Fig. 5 SEM micrographs of as-prepared (AP) and annealed $Y(OH)CO_3$ powders. (AN7) – annealed 1 h at 700 K, (AN) – 1 h at 1100 K and (AN+H) - 1 h at 1100 in hydrogen. The micrographs have the same magnification: × 30 k (left) and × 100 k (right). For (**a**) and (**g**) section also the selected area enlargement has been marked

particles is in the range of 180–210 nm, with an average value of ~200 nm. For powders annealed at 700 K (sample AN7) the particles are somewhat smaller (180–195 nm). The same was also found for powders annealed at higher temperature i.e. at 1100 K where the estimated size range is 165–185 nm. For the same material a final annealing step in flowing hydrogen at 1100 K generates a rather minimal change in the average particle diameter (160–180 nm). In summary, the average particle size of calcined powder particles decreases by about 15% compared with the starting carbonate particles of the as-prepared material. Thus the expected decrease of particle volume is about 35%.

Earlier reports suggest that the final value of the particle size is mostly determined by the concentrations of the yttrium salt and urea in the aqueous solution [11], and also by ageing parameters such as pH and

temperature [12]. From our SEM investigations on powders with different compositions (see Table 1) it was found that as-prepared powder particles have different average sizes. Assuming that all preparation conditions for the synthesized materials were the same, the size variation can be attributed to the introduction of different RE^{3+} dopant. The most pronounced size reduction in comparison to pure yttrium carbonate has been found for particles containing 1% to 3% Sm^{3+}.

The SEM micrographs presented in Fig. 5 indicate that the powder particles have, to some extent, a tendency to agglomerate in an orderly way.

In the course of our SEM experiments different substrates were considered to replace the ''classical'' aluminium and carbon tape sample holder. Powder images were recorded for surfaces such as graphite, alumina or silica film. Micrographs shown in Fig.5 were obtained for particles deposited on thin plates of silica glass (0.5 mm). We assume that the visible regular hexagonal clusters are the result of the specific SEM sample deposition technique. We have to stress that noticeable in Fig. 5, short-range order of particles is not related to particular electrostatic interactions between them or between particles and the glass surface. The existence of small ordered clusters can be associated to the following preparation steps: (i) dispersion of particles in water, (ii) sedimentation by centrifugation of water dispersion and finally, (iii) slow drying of the resulting film on the surface. A different feature has been noticed for SEM images obtained on samples prepared by standard drying of water-dispersed particles on a surface. In these experiments only totally disordered 3D agglomeration of powder particles has been found. We expect that materials based on spherical nanoparticles with homogeneous size can offer valuable building blocks for 2D and 3D superlattice assembly and may be used in the development of thin-film electroluminescent (TFEL) devices [25]. Further investigations are required to find the optimal preparation route as well as possible and practical assembly methods.

One of the additional features observed for thermally treated powders is a change of the particle surface in comparison with the untreated one. The two following micrographs show the typical change for the as-prepared and 1100 K annealed powders.

The particles of all as-prepared powders show very fine surface features that have typical dimensions of only a few nanometers (< 10 nm). In addition, on the surface less visible larger irregular texture elements, forming shell fragments, can be located. A representative picture for the as-prepared powder particles is shown in Fig.6. In this figure separation of all particles is clearly visible, which is characteristic only for powders that were

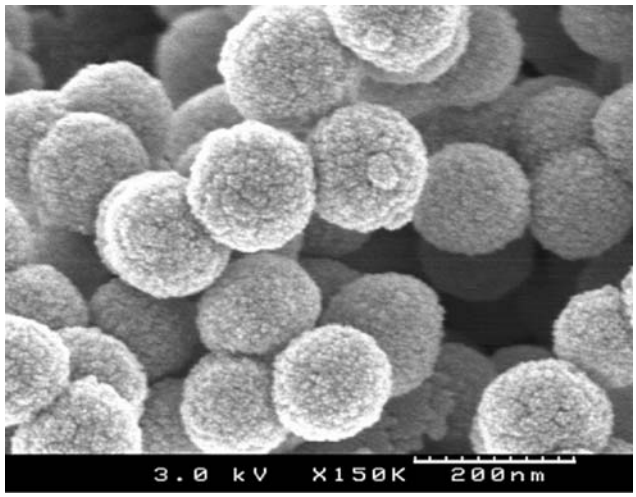

Fig. 6 SEM micrographs of as-prepared $Y(OH)CO_3$:3%Sm particles (sample Sm3-AP)

mechanically stirred during the precipitation process. In contrast when the metal salt assisted urea decomposition has been performed without mechanical stimulation, the process of particle nucleation produced frequently small clusters of surface connected particles (2–5 particles). The final form of groups of particles also suggest that the tendency to nanocluster formation can be attributed to the concluding period of the precipitation process, when it is possible that the pH can reach values close to ~7.6 (the isoelectric point of the precipitate surface). Assuming ''zero charge'' on the particle surface, partial agglomeration is due to the absence of repulsion forces between yttrium carbonate particles. An example of typical clusters is shown in Fig. 7, where small agglomerates of 3, 4 and 5 particles are clearly visible. The large surface texture is an additional feature of these particles. All particles remain spherical, but due to the high temperature treatment, decomposition and crystallization processes are taking place. The average size of formed irregular surface features are in the range of 20–50 nm, which is in excellent agreement with an average size of nanocrystals ($L \approx 35$ nm for Y_2O_3:1%Sm) as has been estimated from the XRD analysis.

Conclusions

Carbonate co-precipitations based on the urea decomposition in elevated temperature of yttrium nitrate and rare earth salts (nitrates and chlorides) in water solutions are a facile and effective method to synthesize very fine and homogeneous spherical particles. In the course of these investigations, we examined the

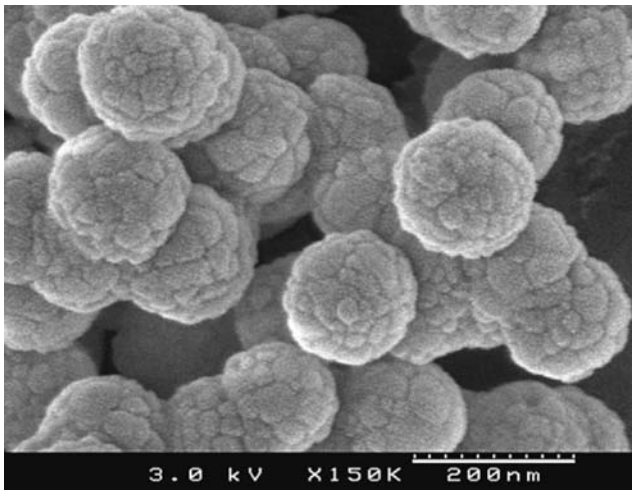

Fig. 7 SEM micrograph of Y_2O_3:1%Sm after two annealing steps in air and in flowing hydrogen at 1100 K for 1 h each (sample Sm1-ANH)

possibility of producing well-defined yttria particles with a broad range of $RE^{3+} \rightarrow Y^{3+}$ substitution. Typically, as-prepared materials are amorphous, but after annealing at temperatures above ~700 K the transitional crystalline phase appears. Crystallization of cubic type yttria and RE-yttria doped particles starts at temperatures above 880 K. Finally, thermally stable nanocrystalline material is formed after annealing at temperatures above 1100 K. The diameter of as-prepared particles is in the range of 180–210 nm as is estimated from SEM micrographs. A decrease of particle size was observed for all RE doped particles. Due to the annealing the average particle size for calcined powders decreases by about 15%. The estimated average crystal size is ~45 nm for pure yttria crystalline particles and 10–30% smaller for RE substituted samples. The cause for this reduction is currently not known and further microstructural investigations are needed. Supplementary heat treatment in flowing hydrogen has a minimal influence on the structural stability in the crystalline powders. The introduction of transition metal ions such as Ti^{4+} for charge compensation of Sm^{2+} in yttria crystal structure is not accommodated within the existing structure, and a separate mixed yttrium oxide-titanium oxide phase is formed.

We have measured the luminescence of all the investigated samples and we have found that all of them exhibit efficient f-f luminescence. This indicates that RE^{3+} ions are incorporated into the lattice. We have also conducted a wide range of up-conversion experiments using 976 nm laser light, co-doping Y_2O_3 with Yb^{3+} and Er^{3+}. The highest efficiency for up-conversion was observed for a 4% and 1% Yb^{3+} and Er^{3+} concentration, respectively. However, there appears to be little variation between the up-conversion properties of the nanoparticles and the bulk material. A detailed account of optical properties of the nanoparticles discussed in this paper will be reported elsewhere.

Acknowledgements The authors thank their colleagues Drs L. Giersig and A. Schindler, NETZSCH-Gerätebau GmbH, for the use of the STA 449 Jupiter thermal analyzer, and Dr S. Stowe, Electron Microscope Unit, Australian National University for the use of the Hitachi S-4500 FESEM. The work was supported in part by Australian Research Council grant A00104371.

References

1. Swamy V, Seifert HJ, Aldinger F (1998) J Alloys Comp 269:201
2. Samsonov GV (1973) The oxide handbook, IFI/Plenum Press, London, p 109
3. Matsuura D (2002) Appl Phys Lett 81:4526
4. Minami T (2002) Solid-State Electronics 47:2237
5. Schmechel R, Kennedy M, von Seggern H, Winkler H, Kolbe M, Fischer RA, Xaomao L, Benker A, Winterer M, Hahn H (2001) J Appl Phys 89:1679
6. Boulon G, Laversenne L, Goutaudier C, Guyot Y, Cohen-Adad MT (2003) J Lumin 102–103:417
7. Fornasiero L, Mix E, Peters V, Petermann K, Hubner G (2000) Ceram Internat 26:598
8. Wittke JP, Ladany I, Yocom PN (1972) J Appl Phys 43:595
9. Pons O, Moll Y, Huignard A, Antic-Fidancev E, Aschehoug P, Viana B, Millon E, Perriere J, Garapon C, Mugnier J (2000) J Lumin 87–89:1115
10. Dassuncao LM, Giolito I, Ionashiro M (1989) Thermochim Acta 137:319
11. Matijevic E, Hsu Wan P (1987) J Coll Inter Sci 118:506
12. Aiken B, Hsu Wan P, Matijevic E (1988) J Am Cer Soc 71:845
13. Duran P, Moure C, Jurado JR (1994) J Mater Sci 29:1940
14. Ji-Guang Li, Ikegami T, Wang Y, Mori T (2002) J Sol State Chem 168:52
15. Dasgupta N, Krishnamoorthy R, Thomas Jacob L (2001) Inter J Inorg Mater 3:143
16. Hao J, Studenikin SA, Cocivera M (2001) J Lumin 93:313
17. Pang Q, Shi J, Liu Y, Xing D, Gong M, Xu N (2003) Mat Sci Eng B103:57
18. Davolos MR, Feliciano S, Pires AM, Marques RFC, Jafelicci M Jr (2003) J Sol State Chem 171:268
19. Shaw WHR, Bordeaux JJ (1955) J Am Chem Soc 77:4729
20. Bates CF, Mesmer RE (1976) In: The hydrolysis of cations. Wiley, New York, p 129
21. Wyckoff RWG (1964) In: Crystal structure, vol 2. Interscience, New York
22. Azarov LV (1968) In: Elements of X-ray crystallography. McGraw-Hill, New York, p 552
23. Subramian MA, Sleight AW (1993) Rare Earth Pyrochlores In: Gschneider KA Jr., Eyring L (eds) Handbook on the physics and chemistry of rare earth, vol 16. Elsevier Science North-Holland, Amsterdam, p 231
24. Tanaka M, Nishisu Y, Kobayashi M, Kurita A, Hanzawa H, Kanematsu Y (2003) J Non-Crys Sol 318:175
25. Ng V, Lee YV, Chen BT, Adeyeye AO (2002) Nanotechnology 13:554